

Article

Incorporation of Mg²⁺/Si⁴⁺ in ZnGa₂O₄:Cr³⁺ to Generate Remarkably Improved Near-Infrared Persistent Luminescence

Shimeng Zhang, Junqing Xiahou, Xudong Sun and Qi Zhu *

Key Laboratory for Anisotropy and Texture of Materials (Ministry of Education), School of Materials Science and Engineering, Northeastern University, Shenyang 110819, China

* Correspondence: zhuq@smm.neu.edu.cn; Tel.: +86-024-8367-2700

Abstract: Near-infrared emitting nano-sized particles of ZnGa_{2-x}(Mg/Si)_xO₄:Cr³⁺ ($x = 0-0.15$, termed as ZGMSO:Cr³⁺) with persistent luminescence were prepared by sol-gel processing followed by calcination. The samples were tested by XRD, TEM, STEM, SAED, Raman, XPS, UV-Vis-NIR, TL, PLE/PL spectroscopy, and persistent luminescence decay analysis. Equimolar incorporation of Mg²⁺ and Si⁴⁺ ions did not change the spindle structure of ZnGa₂O₄ seriously. Most Mg²⁺ ions are more likely to occupy the sites in octahedron, but Si⁴⁺ ions are more likely to occupy the sites in tetrahedron in priority. A broader bandgap, up shift of conduction band minimum, and more anti-defects were found at a higher Mg²⁺/Si⁴⁺ doping concentration. ZGMSO:Cr³⁺ outputs near-infrared emission with a dominated band at 694 nm (²E → ⁴A₂ transition of Cr³⁺), which can last longer than 48 h after the stoppage of UV irradiation. Mg²⁺/Si⁴⁺ doping contributes to a better near-infrared persistent luminescence, and the strongest and the longest NIR afterglow was observed at $x = 0.05$, owing to that the $x = 0.05$ sample has the deepest defects. The synthesized nanoparticles of ZGMSO:Cr³⁺ not only output intense NIR afterglow but also can be recharged by the red light of LED several times, indicating that they are the potential nano probes for bio imaging in living animals.

Keywords: anti-defects; afterglow; bandgap; persistent luminescence; ZnGa₂O₄; Cr³⁺



Citation: Zhang, S.; Xiahou, J.; Sun, X.; Zhu, Q. Incorporation of Mg²⁺/Si⁴⁺ in ZnGa₂O₄:Cr³⁺ to Generate Remarkably Improved Near-Infrared Persistent Luminescence. *Coatings* **2022**, *12*, 1239. <https://doi.org/10.3390/coatings12091239>

Academic Editor: Michelina Catauro

Received: 3 August 2022

Accepted: 22 August 2022

Published: 25 August 2022

Publisher's Note: MDPI stays neutral with regard to jurisdictional claims in published maps and institutional affiliations.



Copyright: © 2022 by the authors. Licensee MDPI, Basel, Switzerland. This article is an open access article distributed under the terms and conditions of the Creative Commons Attribution (CC BY) license (<https://creativecommons.org/licenses/by/4.0/>).

1. Introduction

Cr³⁺-activated zinc gallate (ZnGa₂O₄:Cr³⁺) [1] and Cr³⁺-doped zinc gallogermanate (Zn₃Ga₂GeO₈:Cr³⁺) [2,3] spinel phosphors are the new favorites in persistent luminescence materials and attract tremendous attention, mainly due to their near-infrared (NIR) emissions at ~700 nm (the spin forbidden ²E → ⁴A₂ transition of Cr³⁺) and ~650–1600 nm (the spin-allowed ⁴T₂ → ⁴A₂ transition of Cr³⁺), that would last for a long time with several or dozens of hours after removing the light source. Recently, functionalized NIR-emitting persistent luminescent nanoparticles of ZnGa₂O₄:Cr³⁺ and Zn₃Ga₂GeO₈:Cr³⁺ with long lasting afterglow have been successfully synthesized for bio-imaging in living animals [4–14], mainly due to their two advantages: (1) the long-lasting afterglow feature permits detection without external illumination, which can eliminate the noise from the background because of in situ excitation; (2) the NIR emission is beneficial for whole body imaging of living animals because its ratio of signal to noise is high and the penetration is deep. However, for practical applications of the NIR persistent phosphors, the effective afterglow signal rather than the very weak luminescence signal may last for several hours, and the optical materials need to be effectively activated by visible light. Therefore, increased attention has been paid to the improvement of NIR persistent luminescence of spinel phosphors through compositional modification [15–20].

It has been predicted that any combination of ions including alkaline earth, lanthanide or Li⁺ ions in ZnGa₂O₄:Cr³⁺ and Zn₃Ga₂GeO₈:Cr³⁺ may possibly produce materials with remarkable NIR persistent luminescence, because the incorporation of foreign ions would increase the efficient electron traps [2,21–23]. More recently, Sn⁴⁺-doped ZnGa₂O₄:Cr³⁺ [24],

Pr^{3+} [5], Bi^{3+} [25], Eu^{3+} [26], $\text{Yb}^{3+}/\text{Er}^{3+}$ [27] doped zinc gallogermanate persistent luminescent materials were synthesized, and the improved NIR persistent luminescence is attributed to distorted octahedral sites arising from foreign ions occupying six-coordinated Ga site [28]. However, the reports on incorporation of two different valence ions in $\text{ZnGa}_2\text{O}_4:\text{Cr}^{3+}$ at the same time are rather limited because of their complex occupation on Zn site (four-coordinated) or Ga site (six-coordinated). But it has ability to potentially regulate the effective defects which are beneficial to the improvement of NIR persistent luminescence. In this work, equimolar Mg^{2+} and Si^{4+} ions were introduced in $\text{ZnGa}_2\text{O}_4:\text{Cr}^{3+}$ through occupying both the four- and six- coordinated sites, which increase the efficient electron traps by local microstructure regulation, thus generating remarkable improved near-infrared persistent luminescence. The local structure and the near-infrared persistent luminescence of $\text{ZnGa}_{2-x}(\text{Mg}/\text{Si})_x\text{O}_4:\text{Cr}^{3+}$ ($x = 0-0.15$, termed as ZGMSO: Cr^{3+}) were investigated via detailed characterizations of X-ray diffractometry (XRD), transmission electron microscopy (TEM), STEM, SAED, Raman, X-ray photoelectron spectrometer (XPS), UV-Vis-NIR, Thermoluminescence (TL), PLE/PL spectroscopy, and persistent luminescence decay analysis. The results of this work may have wide implications on other optical materials with persistent luminescence.

2. Experimental Section

2.1. Synthesis

The starting materials of $\text{Zn}(\text{NO}_3)_2 \cdot 6\text{H}_2\text{O}$, $\text{Mg}(\text{NO}_3)_2 \cdot 6\text{H}_2\text{O}$, $\text{Cr}(\text{NO}_3)_3 \cdot 9\text{H}_2\text{O}$, SiO_2 , and Ga_2O_3 , were purchased from Sinopharm (Shanghai, China) with the purity of 99.99%. Ga_2O_3 was dissolved in nitric acid solution. ZGMSO: Cr^{3+} samples were prepared by sol-gel processing in the presence of trimethylaminomethane (THAM), followed by calcinations at 1000°C . The molar ratio of THAM to total cationic ions is maintained at 2:1, and the Cr^{3+} content is fixed at 0.5 at.%, substituting for Ga^{3+} .

2.2. Characterization Techniques

X-ray diffractometry (XRD, Model SmartLab, Rigaku, Tokyo, Japan) was used for phase identification, which was performed by operating at 40 kV/40 mA using nickel filtered $\text{Cu K}\alpha$ radiation and a scanning speed of $6.0^\circ 2\theta/\text{min}$. A Raman microscope (Model R-XploRA Plus, Horiba, Kyoto, Japan) was used for Raman scattering measurements, using the with a 532 nm He-Ne laser as the excitation source. At the sample, the laser power was fixed at 49.1 mW. An X-ray photoelectron spectrometer (Model Axis Supra, Kratos Analytical Ltd., Manchester, UK) was used for the data of X-ray photoelectron spectroscopy (XPS) using the monochromatized $\text{Al K}\alpha$ X-ray radiation. At room temperature, the measurements were performed using an ultrahigh vacuum chamber with a base pressure below 3×10^{-9} Torr. C 1 s (284.8 eV) of carbon impurities was used as reference to calibrate binding energies. Transmission electron microscopy (TEM, Model JEM-2000FX, JEOL, Tokyo, Japan) was used to test the morphologies of the products. The composition of the product was analyzed by inductively coupled plasma (ICP) spectroscopy (Model Optima 8300 and Optima 4300, Perkin Elmer, Shelton, CT, USA) with a detection limit of 0.01 wt.%. UV-Vis-NIR spectrophotometer (UV-3600 Plus, Shimadzu, Kyoto, Japan) was used for diffuse reflectance spectra of the samples at room temperature. A spectrometer (Model FJ427A TL, Beijing Nuclear Instrument Factory, Beijing, China) was used to test the glow curves of the samples with a heating rate of $1^\circ\text{C}\cdot\text{s}^{-1}$ on after exposure to UV light for 5 min at room temperature. FP-8600 fluorospectrophotometer (Jasco, Tokyo, Japan) was used to analyze the photoluminescence of the phosphors, and Horiba JY FL3-21 (Horiba, Kyoto, Japan) was used to detect the persistent luminescence signals.

For Rietveld refinement, the data were collected through a step-scan mode over the 2θ range of $15^\circ-120^\circ$, using a step interval of 0.02° and a counting time of 1 s per step. TOPAS 4.2 software was carried out for the Rietveld refinement of the XRD patterns.

3. Results and Discussion

3.1. Synthesis, Morphology and Local Structure

XRD pattern of the prepared ZGMSO:Cr³⁺ ($x = 0-0.20$) calcined at 1000 °C are displayed in Figure 1. The diffractions of the samples with $x = 0-0.15$ are well-indexed to spinel structured ZnGa₂O₄ (JCPDS No. 38–1240). There are two kinds of sites for cationic ions in the crystal structure, which are A site for Zn²⁺ in a tetrahedron surrounded by four oxygen anions, and B site for Ga³⁺ in an octahedron surrounded by six oxygen anions, respectively [28]. Appearance of a small trace of another phase corresponding to Zn₂SiO₄ (JCPDS No. 85–0453) takes place with the x value reaching 0.20, along with main phase of ZnGa₂O₄. The results indicates that the incorporation threshold of Mg²⁺ and Si⁴⁺ in ZnGa₂O₄ is 15% ($x = 0.15$). Inductively coupled plasma (ICP) spectroscopy was employed to analyze the composition of the product, and the results of chemical analysis for ZGMSO:Cr³⁺ ($x = 0.01, 0.05, 0.15$) are shown in Table 1. Elemental analysis identified ZnGa_{2.08}(Mg²⁺/Si⁴⁺)_{0.0095}O_{4.14}:0.0048Cr³⁺ for $x = 0.01$ sample, ZnGa_{2.05}(Mg²⁺/Si⁴⁺)_{0.046}O_{4.15}:0.0049Cr³⁺ for $x = 0.05$ sample, and ZnGa_{1.97}(Mg²⁺/Si⁴⁺)_{0.154}O_{4.19}:0.0047Cr³⁺ for $x = 0.15$ sample, respectively. The results indicate that the composition of the prepared samples is very close to the stated objective one. Figure 2a shows the typical Rietveld structure refinements of $x = 0.05$ sample, using the standard ZnGa₂O₄ as initial model of crystal structure. Comparing the calculated and the experimental data finds that all the diffraction peaks are well matching, in absence of other impurity in the sample. The calculated values of residual factor are $R_{wp} = 10.63\%$, $R_p = 6.66\%$, $R_{exp} = 5.92\%$ and $\chi^2 = 1.80$. The acceptable reliability factors further confirmed that the sample is a single phase, which crystallizes in a spinel structure (cubic) with the space group of Fd-3m. Figure 2b shows Morphology of $x = 0.05$ sample under TEM observation, that indicates that the sample entirely consist of nanoparticles, with the sizes ranging from ~20 to ~100 nm. The SAED analysis (Figure 2c) suggested that the nanoparticles are single crystalline and exhibit excellent crystallinity. The calculated plain spacings from SAED pattern are assigned to the (220) and (422) plains of ZnGa₂O₄ (JCPDS No. 38–1240), indicating the formation of spinel structured solid solution. Elemental mapping results are shown in Figure 3, finding that all cationic elements are distributed among the particles, and all the elements outline the particle morphology consistent with that in Figure 2b, suggesting that the nanoparticles are homogeneous solid solutions.

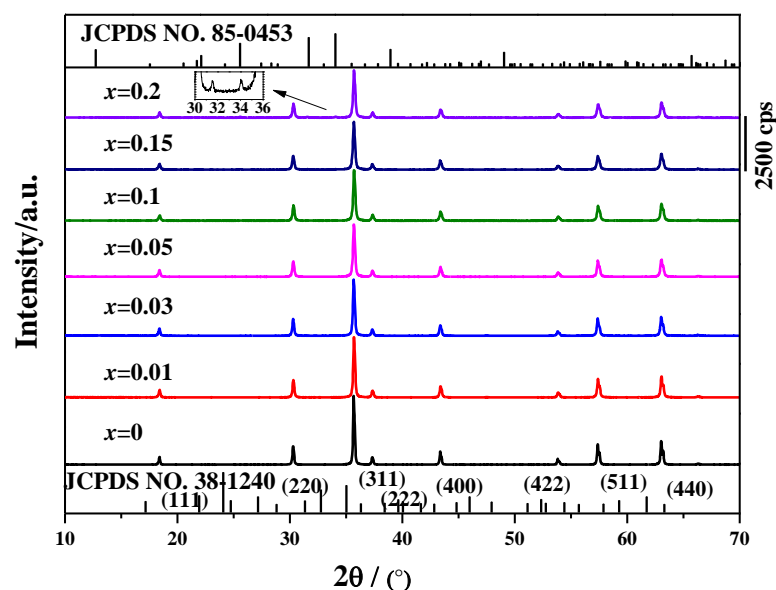


Figure 1. XRD pattern for the prepared ZGMSO:Cr³⁺ ($x = 0-0.20$) calcined at 1000 °C.

Table 1. Results of chemical analysis for ZGMSO:Cr³⁺ ($x = 0.01, 0.05, 0.15$).

x	Chemical Analysis (wt.%)					Chemical Formula
	Zn	Ga	Mg	Si	Cr	
0.01	23.4	51.9	0.04	0.05	0.09	ZnGa _{2.08} (Mg ²⁺ /Si ⁴⁺) _{0.0095} O _{4.14} :0.0048Cr ³⁺
0.05	23.3	51.1	0.22	0.21	0.09	ZnGa _{2.05} (Mg ²⁺ /Si ⁴⁺) _{0.046} O _{4.15} :0.0049Cr ³⁺
0.15	24.2	49.2	0.66	0.80	0.09	ZnGa _{1.97} (Mg ²⁺ /Si ⁴⁺) _{0.154} O _{4.19} :0.0047Cr ³⁺

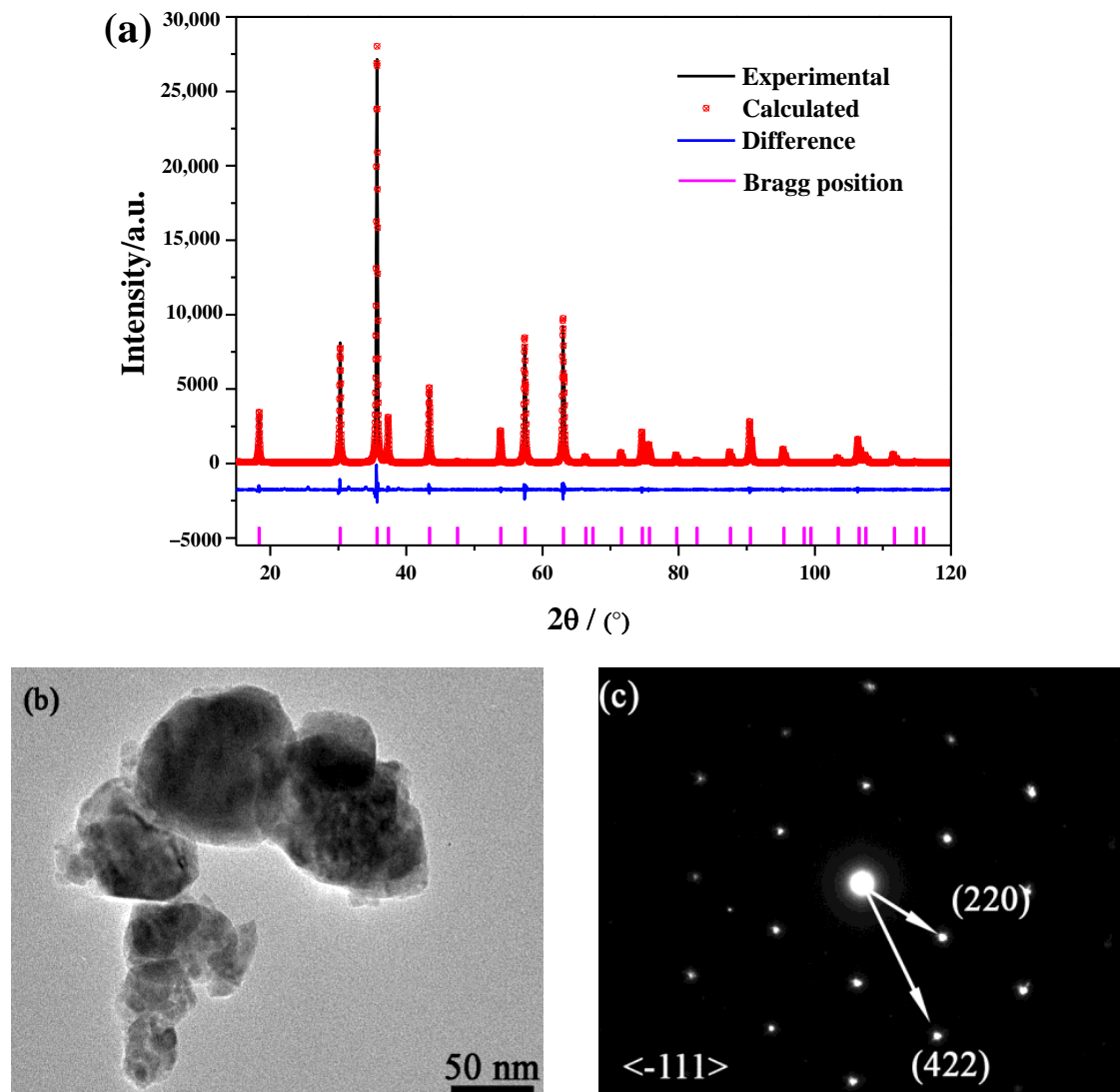
**Figure 2.** (a) Rietveld refinements, (b) TEM image, and (c) SAED patterns of ZGMSO:Cr³⁺ ($x = 0.05$ sample).

Figure 4a presents the X-ray photoelectron spectroscopy (XPS) survey spectra (Figure 4a). The results match well to the elemental mapping results, because other elements were not detected except for the original components and contaminating carbon. High-resolution XPS spectra of Zn 2p_{3/2}, Ga 2p_{3/2}, Mg 1s, Si 2p core levels for ZGMSO:Cr³⁺ ($x = 0-0.15$) were analyzed in Figure 4b–e, which reveals the effect of incorporation of Mg²⁺/Si⁴⁺ on the microstructure. Due to a few of tetrahedral Ga and octahedral Zn sites arising from anti-defects appear in spinel-structured zinc gallate [1], a small amount of anti-site Zn²⁺ and Ga³⁺ contribute to the asymmetric XPS spectra, which may be fitted using a bi-Gaussian function (Figure 4b,c). Due to the binding energy of cationic ions in the tetrahedral sites is

smaller than that in the octahedral sites, the fitting binding energy at higher is assigned to the cationic ions occupying octahedral while the lower value is assigned to the cationic ions occupying tetrahedral sites [29]. Although Zn^{2+} ions in tetrahedron and Ga^{3+} in octahedron takes the dominate role, increasing the doping content of $\text{Mg}^{2+}/\text{Si}^{4+}$ (x value) induces more Zn^{2+} ions being in octahedron while more Ga^{3+} ions being in tetrahedron (Tables S1 and S2), indicating more anti-defects appear. Since most Mg^{2+} ions are in octahedron, the fitted area ratio of the peak at the higher energy (~ 1304 eV) takes the dominate role (Figure 4d and Table S3). When the x increases from 0.01 to 0.15 (Table S3), the fitted area ratio of the peak at the lower value of ~ 1300 eV increases and then takes the dominate role, indicating more Mg^{2+} ions occupying tetrahedral sites at a higher $\text{Mg}^{2+}/\text{Si}^{4+}$ doping content. However, most Si^{4+} ions are in tetrahedron, because the fitted area ratio of the peak at the lower value of ~ 105 eV is larger (Figure 4e and Table S4). Since the ionic radii of Si^{4+} (0.026 nm for four coordination and 0.040 nm for six coordination) is much smaller than that of Zn^{2+} (0.060 nm for four coordination) and that of Ga^{3+} (0.062 nm for six coordination) [30], Si^{4+} ions are indeed in both the tetrahedron (Zn sites) and octahedron (Ga sites). Increasing the x value did not significantly affect the occupation ratio of Si^{4+} in tetrahedral and octahedral sites. The above results suggest: (1) Si^{4+} ions occupy the tetrahedral sites in ZnGa_2O_4 in priority and their occupation exhibits an independence on the $\text{Mg}^{2+}/\text{Si}^{4+}$ doping content (x value); (2) more incorporation of $\text{Mg}^{2+}/\text{Si}^{4+}$ would induce more anti-defects appear.

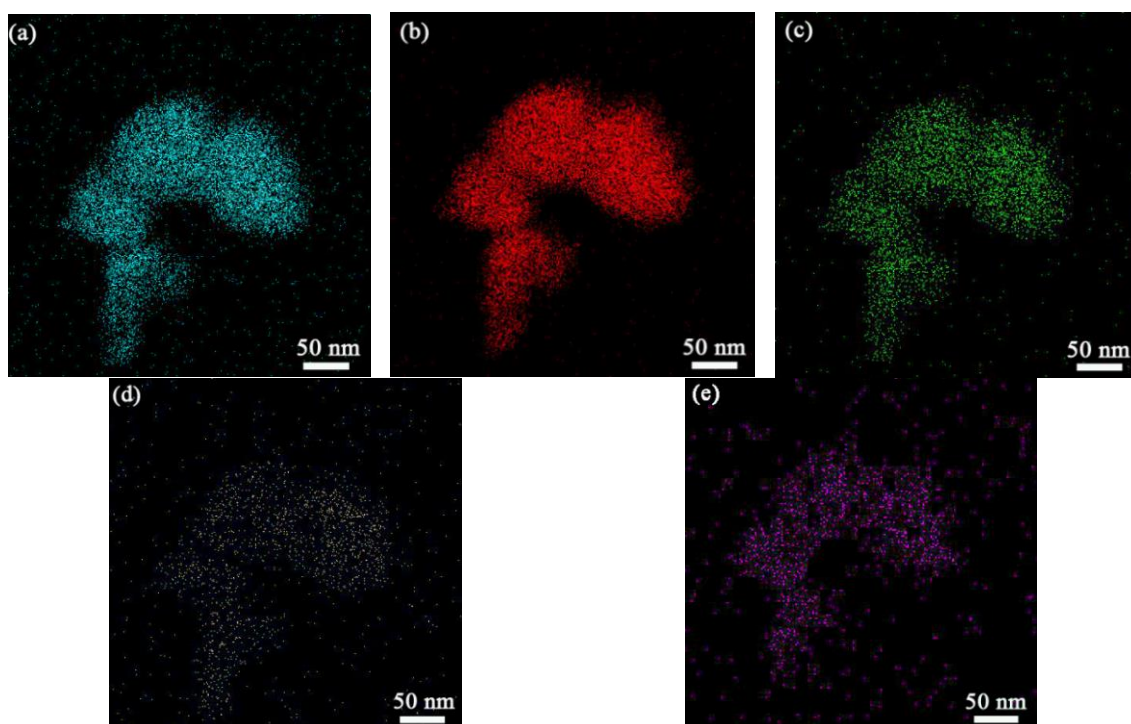


Figure 3. Element distribution of $\text{ZGMSO}:\text{Cr}^{3+}$ ($x = 0.05$ sample), with (a) Zn, (b) Ga, (c) Mg, (d) Si, (e) Cr.

Raman spectra of $\text{ZGMSO}:\text{Cr}^{3+}$ ($x = 0-0.15$) are exhibited in Figure 5. For the spinel structure, group theory predicts the following phonon modes, $\Gamma = A_{1g} + E_g + T_{1g} + 3T_{2g} + 2A_{2u} + 2E_u + 5T_{1u} + 2T_{2u}$ [31]. Gorkom et al. [32] reported that the Raman peak at ~ 714 cm^{-1} is assigned to A_{1g} Raman-active modes ($k = 0$), while the peak at ~ 610 cm^{-1} is assigned to T_{2g} Raman-active modes ($k = 0$). In this work, the Raman peaks at ~ 610 and ~ 714 cm^{-1} are clearly observed for ZnGa_2O_4 ($x = 0$ sample), which indicates there are a large amount of ZnO_4 groups with symmetric stretching vibrations [32,33]. However, the intensity of Raman peaks at ~ 610 and ~ 714 cm^{-1} weakens with increasing the x up to 0.15. More $\text{Mg}^{2+}/\text{Si}^{4+}$ doping (larger x value) would induce more Si^{4+} and Mg^{2+} ions occupying

tetrahedral sites, along with more anti-defects of Ga^{3+} ions in tetrahedral sites, so a few of ZnO_4 groups in symmetric status transformed into ZnO_4 groups in distorted status, which contributes to the weakened Raman peaks.

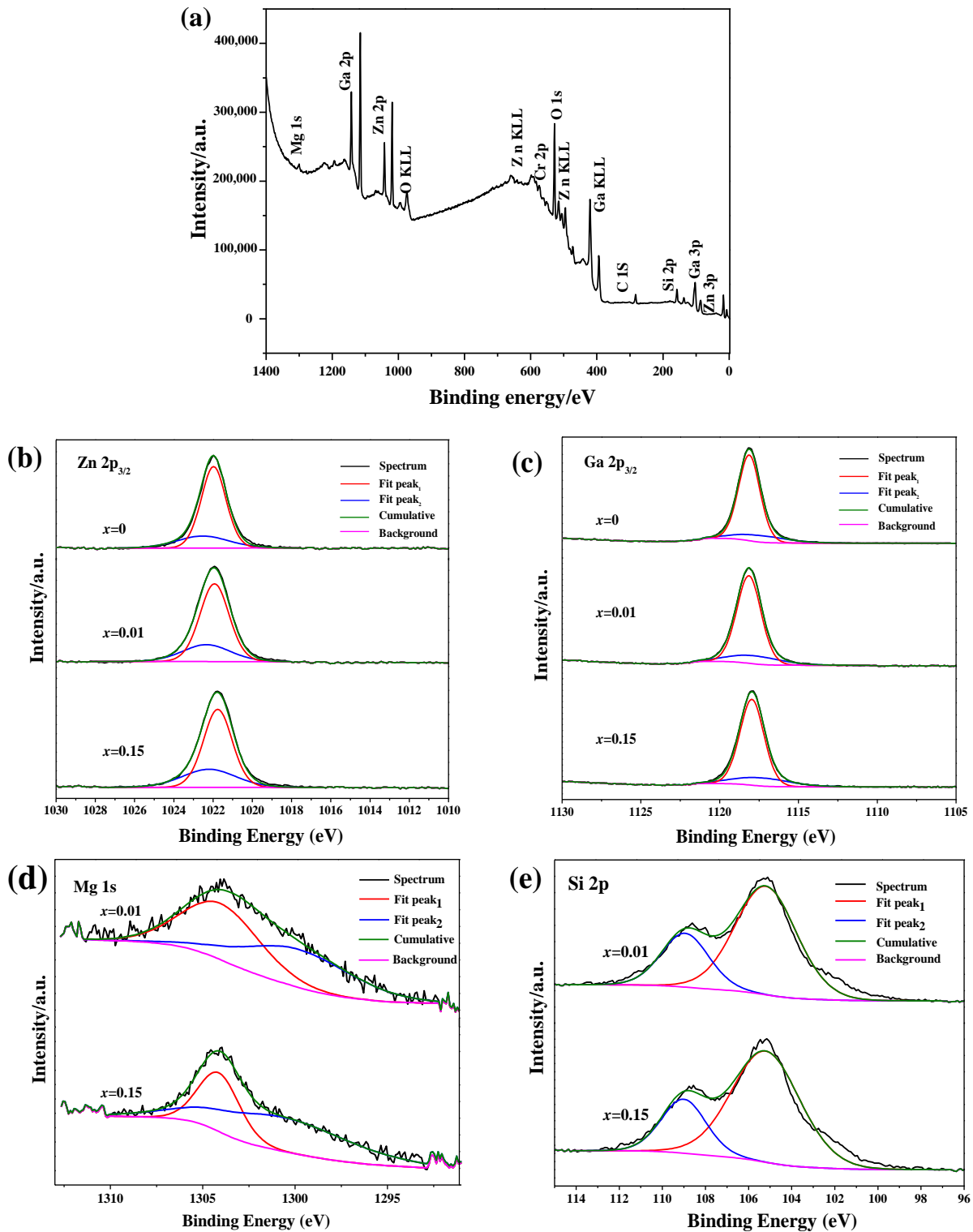


Figure 4. (a) XPS survey spectrum of ZGMSO:Cr³⁺ ($x = 0.05$ sample) and (b–e) high-resolution XPS spectra of ZGMSO:Cr³⁺ ($x = 0–0.15$): (b) Zn 2p_{3/2}, (c) Ga 2p_{3/2}, (d) Mg 1s, (e) Si 2p.

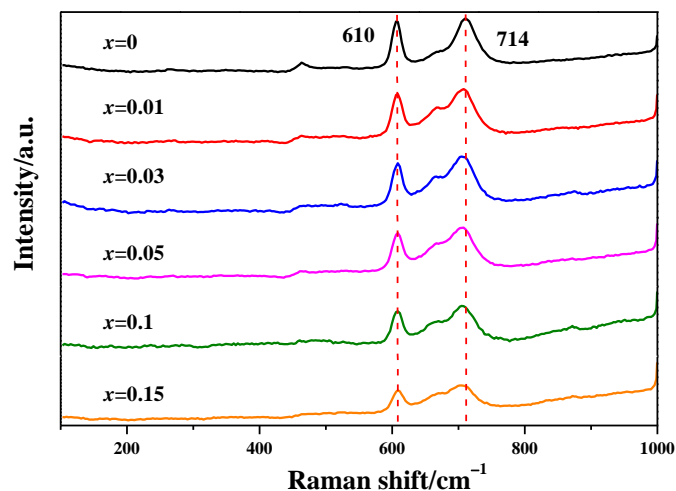


Figure 5. Raman spectra of the prepared ZGMSO:Cr³⁺ ($x = 0$ – 0.15) calcined at $1000\text{ }^{\circ}\text{C}$.

3.2. Photoluminescence and NIR Persistent Luminescence of ZGMSO:Cr³⁺

Figure 6a displays the photoluminescence excitation (PLE) and emission (PL) spectra of ZnGa₂O₄:Cr³⁺ and ZGMSO:Cr³⁺ (taking $x = 0.05$ sample as an example) at room temperature. In the PLE spectra, three excitation bands are found by being monitored at a near-infrared (NIR) wavelength of 694 nm. The strongest excitation bands at the wavelength range from 220 to 320 nm, are arising from the overlap of VB \rightarrow CB transition and ${}^4A_2 \rightarrow {}^4T_1$ (4P) transition of Cr³⁺ [1,2]. While the excitation peaks at 410 and 565 nm are assigned to ${}^4A_2 \rightarrow {}^4T_1$ (4F) transition and ${}^4A_2 \rightarrow {}^4T_2$ transition of Cr³⁺, respectively [1,2,14], indicating the samples can be excited by visible light, such as blue and orange red light, except for the UV irradiation. Under the 265 nm UV excitation, the samples exhibit a near-infrared (NIR) emission with the maximum at 694 nm, which is arising from the ${}^2E \rightarrow {}^4A_2$ transition of Cr³⁺, this is mainly due to Cr³⁺ ions occupying the distorted octahedrons. It is interesting to find that incorporation of Mg²⁺/Si⁴⁺ ions, leads to the NIR emission intensity at 694 nm increasing by $\sim 23\%$ and the maximum peak of the strongest UV excitation band shifting from 256 to 265 nm, through comparing with the excitation and emission spectra of ZnGa₂O₄:Cr³⁺ and ZGMSO:Cr³⁺ (Figure 6a). The NIR persistent-luminescence decay curves of ZnGa₂O₄:Cr³⁺ and ZGMSO:Cr³⁺ are compared in Figure 6b, which were monitored at 694 nm after UV light irradiation for 300 s at room temperature. Both of ZnGa₂O₄:Cr³⁺ and ZGMSO:Cr³⁺ could output strong NIR afterglow that lasting more than 7200 s, but ZGMSO:Cr³⁺ exhibits much more intense NIR afterglow than that of ZnGa₂O₄:Cr³⁺ and thus having a longer afterglow time, which indicates that Mg²⁺/Si⁴⁺ doping contributes to an improved NIR persistent luminescence. The persistent luminescence spectra of ZGMSO:Cr³⁺ with various durations confirmed that the NIR signal of afterglow can still be detected after removing the UV light source at 48 h (2880 min, Figure 6c). The appearance of NIR afterglow in Figure 6e directly shows that intense afterglow of ZGMSO:Cr³⁺ can last longer than 240 min, which is much stronger than that of ZnGa₂O₄:Cr³⁺. Since ZGMSO:Cr³⁺ can also be excited by visible light, it was second in situ excited under a red-light lamp for 120 s, and repeated signal of NIR afterglow was observed after removing the excitation. The persistent luminescence spectra of ZGMSO:Cr³⁺ with various durations indicate that the repeated signal of afterglow can last more than three hours (Figure 6d), while the appearances of NIR afterglow in Figure 6e directly show that the repeated signal of afterglow can last more than four hours and exhibit priority to that of ZnGa₂O₄:Cr³⁺. Therefore, it can be inferred that ZGMSO:Cr³⁺ sample possesses an excellent NIR persistent luminescence property and can be repeatedly recharge by red LED light. Since incorporation of Mg²⁺/Si⁴⁺ ions in ZnGa₂O₄:Cr³⁺ contributes to the electrons traps which can store UV and visible light [14,24], the prepared samples exhibited rechargeable

ability for UV light and red LED light. In the following section, the influence of Mg^{2+}/Si^{4+} doping on the NIR persistent luminescence would be investigated in detail.

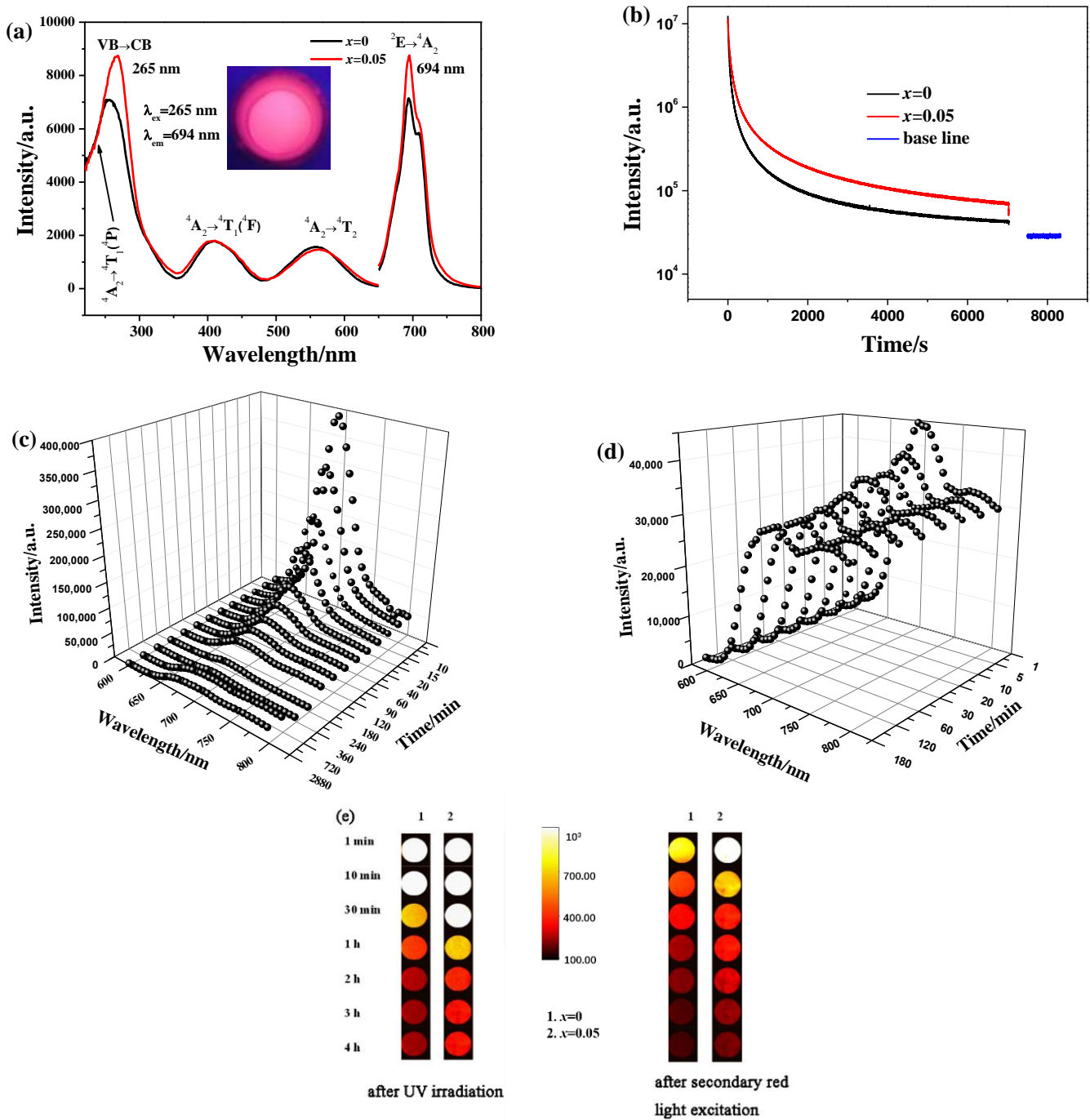


Figure 6. (a) PLE/PL spectra and (b) NIR persistent luminescence decay curves (monitored at 694 nm, 5-min excitation at 254-nm UV light illumination) of $x = 0$ and $x = 0.05$ samples. (c,d) are persistent luminescence spectra of $x = 0.05$ sample with various durations after stopping UV light and secondary excitation with a red light from a LED lamp. (e) is appearance of NIR afterglow of $x = 0.05$ sample with various durations obtained by a Kodak In Vivo Imaging System FX Pro at different times after removing UV irradiation for 5 min and the appearance of recharging NIR afterglow through a secondary excitation of red light.

3.3. Effects of Mg^{2+}/Si^{4+} Doping on the NIR Persistent Luminescence and Mechanism

Figure 7a estimates the bandgap energies of ZGMSO (the host of ZGMSO:Cr³⁺) with various x values, which were determined by a UV-Vis-NIR spectrophotometer. The absorption coefficient (α) and incident photon energy ($h\nu$) follows the relationship as $\alpha = B_d(h\nu - E_g)^{1/2}$, where B_d is the absorption constant and E_g is the bandgap energy [34]. Figure 7a shows the relationship of $(A h\nu)^2$ versus $h\nu$ based on the spectral data. Bandgaps of 4.65 eV for $x = 0$, 4.70 eV for $x = 0.05$, and 4.77 eV for $x = 0.15$ are obtained by extrapolating the linear parts of the curves, which indicates that a higher x value induces a broader bandgap. Figure 7b presents the valence-band XPS spectra, which finds that all the samples have the almost the same edges of the maximum energy at about 2.88 eV. Therefore, the conduction band minimum (CBM) can be calculated from the data of bandgap and valence-band maximum (VBM), and the results are -1.78 eV for $x = 0$, -1.82 eV for $x = 0.05$, and -1.89 eV for $x = 0.15$, respectively. Figure 7c shows TL glow curves of ZGMSO:Cr³⁺ with various x values, and only one main peak ranging from 25 °C (298 K) to 300 °C (573 K) was observed. The main peak temperature of the TL glow curves are summarized in Table 2. Increasing the x value from 0 to 0.05 results in the temperature of peak maximum increasing from 105 °C (378 K) to 128 °C (401 K). Further increasing the x value from 0.05 to 0.15 only yields a slightly decrease with the maximum of the peak being 127 °C (400 K) and 124 °C (397 K) for $x = 0.10$ and $x = 0.15$, respectively. The electron-trap depths of ZGMSO:Cr³⁺ samples can be estimated from the following equation as $E = T_m/500$ [14], where T_m is the peak maximum in TL curves. The electron-trap depth calculated from the TL peaks increases from 0.756 to 0.802 eV with elevating the x value from 0 to 0.05. While the electron-trap depths exhibit a very small reduction by further elevating the x value up to 0.15.

Through the combination of the above results, a schematic illustration of the energy level was constructed in Figure 8. Since the 4T_1 (4P) level of Cr³⁺ is broad and it locates partly in the bandgap and partly in the conduction band (CB), the excitation bands arising from the VB \rightarrow CB transition and the $^4A_2 \rightarrow ^4T_1$ (4P) transition of Cr³⁺ overlap, which thus contributes to the strongest excitation band at the wavelength ranging from 220 to 320 nm (Figure 6a). More Mg^{2+}/Si^{4+} incorporation (larger x value) induces the up shift of CBM, so more parts of the 4T_1 (4P) level appear in the bandgap that are near the CBM (Figure 8). The separation of CB and 4T_1 (4P) level contributes to the red shift of the maximum peak of the strongest UV excitation band. Additionally, due to more part of 4T_1 (4P) level breaks away from CB, more excited electrons leap into the 4T_1 (4P) level rather than the CB, which results in more excited electrons going from 4T_1 (4P) level to 2E level through nonradiative transition and thus contributing to the enhanced emission intensity at 694 nm ($^2E \rightarrow ^4A_2$ transition of Cr³⁺, Figure 6a). Since traps with deep trap depth are not easy to be emptied at room temperature, the sample having deeper traps usually exhibit more intense and longer afterglow. Therefore, $x = 0.05$ sample exhibits the most intense and the longest persistent luminescence, owing to its deepest defects. Since the $x = 0.10$ sample and $x = 0.15$ sample have the trap depth close to that of $x = 0.05$ sample, they exhibit the similar persistent luminescence to that of $x = 0.05$ sample (Figure 9). Previous literatures reported that anti-defects play the role as the electron traps that can capture the excited electrons, so they would contribute to the improved persistent luminescence [35–37]. Here, more incorporation of Mg^{2+}/Si^{4+} resulted in more anti-defects, which thus contributed to the improved NIR persistent luminescence. However, Si^{4+} ions occupy the tetrahedral sites (Zn sites) in ZnGa₂O₄ in priority, which leads to the appearance of Ga vacancy with three negative charges and Si^{4+} in Zn sites with two positive charges. These defects contribute to the electron traps with a deeper depth more than ~ 1.0 eV [28,38,39], where the captured electrons cannot easily escape at room temperature and thus contributes to the worse NIR persistent luminescence. Therefore, the most intense and the longest persistent luminescence was observed for $x = 0.05$ sample, which are the comprehensive outcome from the anti-defects and the defects arising from Si^{4+} ions occupying the tetrahedral sites.

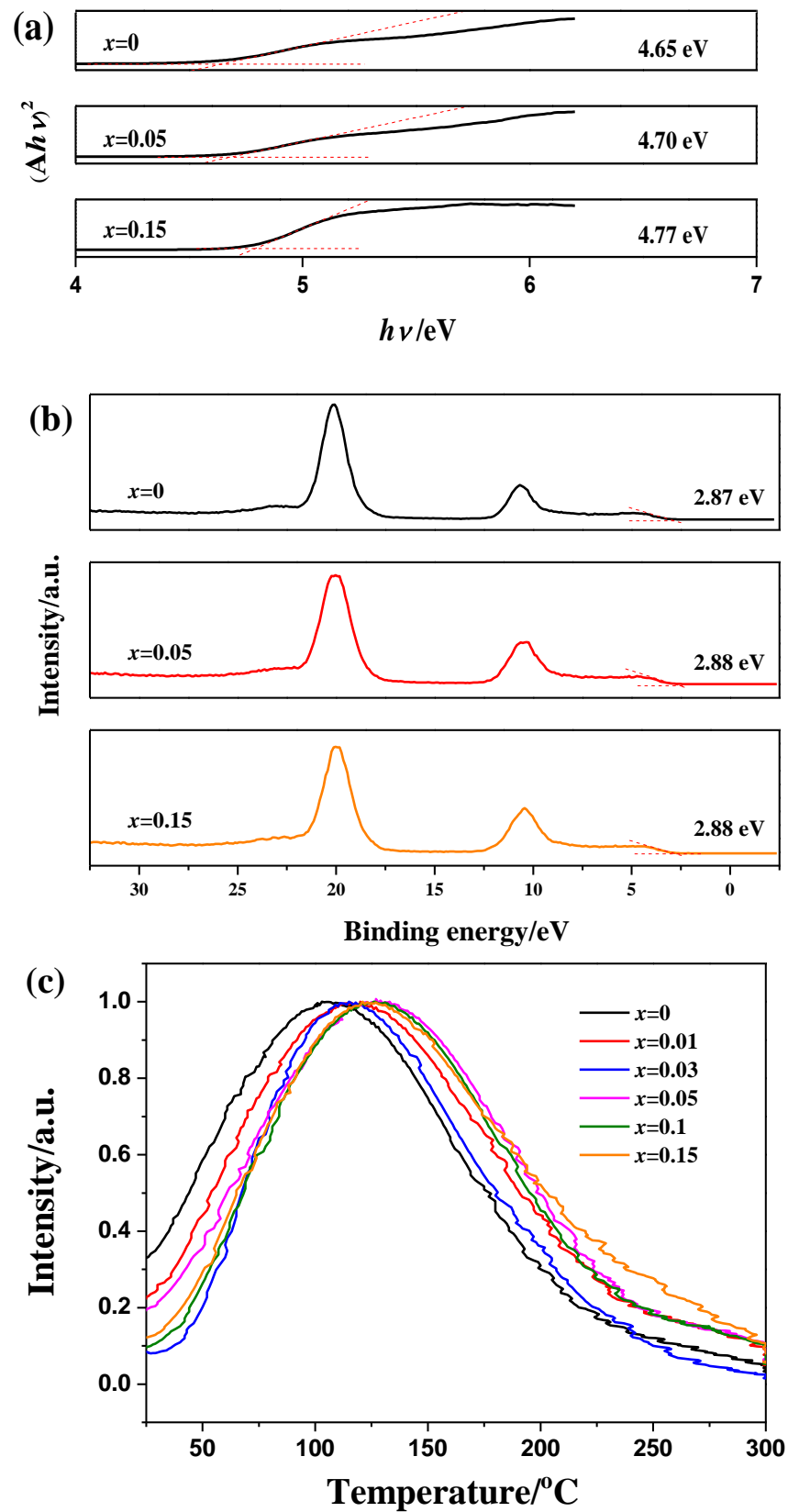


Figure 7. (a) Determination of bandgap energies, (b) Valence-band XPS spectra, and (c) TL glow curves of ZGMSO:Cr³⁺ (x = 0–0.15).

Table 2. Main peak temperatures of the TL glow curves and estimated trap depths.

x	Peak Temperature (°C)	Trap Depth (eV)
0	105	0.756
0.01	114	0.774
0.03	117	0.780
0.05	128	0.802
0.10	127	0.800
0.15	124	0.794

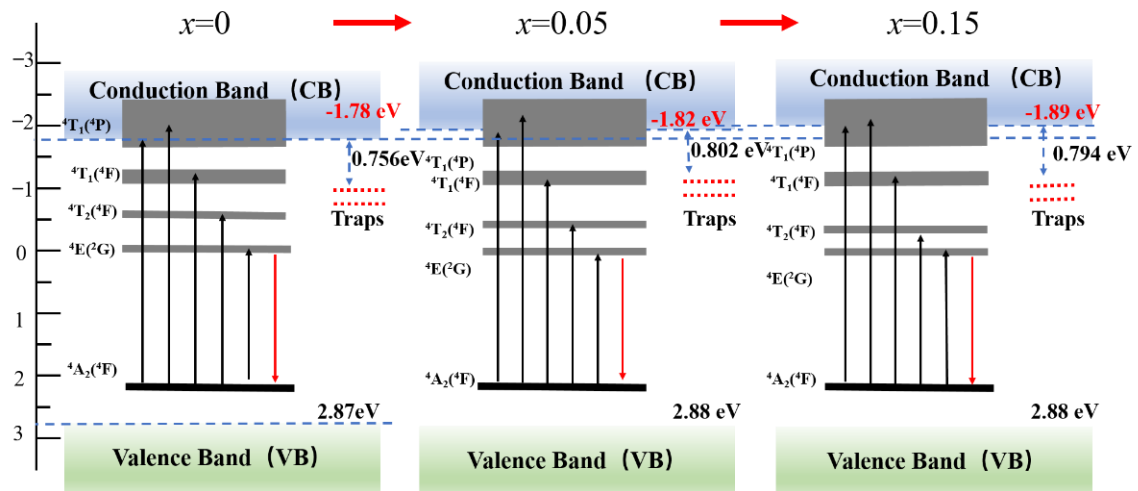


Figure 8. Schematic illustration of energy level diagram.

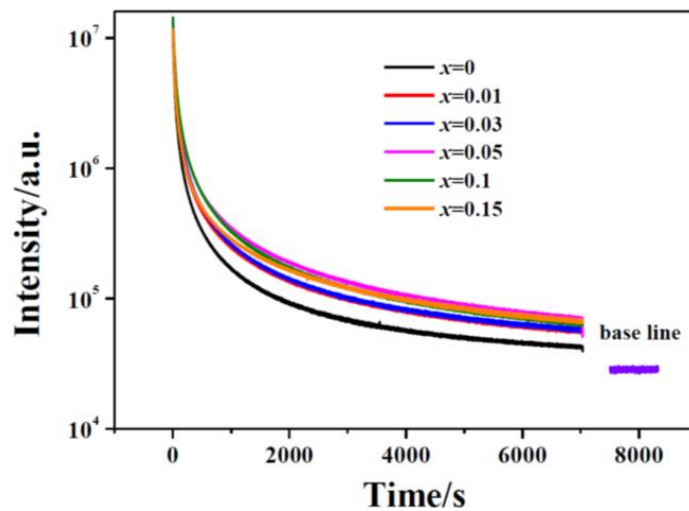


Figure 9. NIR persistent luminescence decay curves of ZGMSO:Cr³⁺ ($x = 0–0.15$).

4. Conclusions

In this work, nano-sized particles of $ZnGa_{2-x}(Mg/Si)_xO_4:Cr^{3+}$ ($x = 0–0.15$, termed as ZGMSO:Cr³⁺) were prepared by sol-gel processing, which were then calcined at 1000 °C. The nanoparticles are single crystalline and well crystallized. Incorporation of equimolar Mg²⁺ and Si⁴⁺ ions did not significantly affect the spindle structure of ZnGa₂O₄. Most Mg²⁺ ions occupy the octahedral sites, but more Mg²⁺ ions occupying tetrahedral sites at a higher Mg²⁺/Si⁴⁺ doping content. Si⁴⁺ ions occupy the tetrahedral sites in priority, which are independent on the Mg²⁺/Si⁴⁺ doping content. More incorporation of Mg²⁺/Si⁴⁺

contributes to broader bandgap, up shift of conduction band minimum, and increased anti-defects. Under the UV excitation, ZGMSO:Cr³⁺ exhibits a near-infrared (NIR) emission with the maximum at 694 nm, which is arising from the ²E → ⁴A₂ transition of Cr³⁺, because Cr³⁺ ions are in the distorted octahedrons. Mg²⁺/Si⁴⁺ doping contributes to an improved NIR persistent luminescence, and the most intense and the longest NIR afterglow was observed for x = 0.05 sample, owing to its deepest defects. The best sample possesses an excellent NIR long-lasting luminescence with intense NIR signal of afterglow more than 48 h and can be rechargeable by a red light of LED lamp. The prepared persistent-luminescence phosphors are suitable for applications in long-term in vivo imaging, and they imaging signal can be repeated in vivo through in situ recharge with external excitation of a red LED lamp.

Supplementary Materials: The following supporting information can be downloaded at: <https://www.mdpi.com/article/10.3390/coatings12091239/s1>, Table S1: The binding energies of the Zn 2p_{3/2} core-levels of ZGMSO:Cr³⁺, Table S2: The binding energies of the Ga 2p_{3/2} core-levels of ZGMSO:Cr³⁺, Table S3: The binding energies of the Mg 1s core-levels of ZGMSO:Cr³⁺, Table S4: The binding energies of the Si 2p core-levels of ZGMSO:Cr³⁺.

Author Contributions: S.Z.: data curation, formal analysis, writing—original draft. J.X.: data curation, formal analysis. X.S.: data curation, formal analysis. Q.Z.: resources, supervision, conceptualization, writing—review and editing, conceptualization. All authors have read and agreed to the published version of the manuscript.

Funding: Natural Science Foundation of Liaoning Province (Grant No. 2020-MS-081) and the National Natural Science Foundation of China (Grant No. 51302032).

Institutional Review Board Statement: Not applicable.

Informed Consent Statement: Not applicable.

Data Availability Statement: Data available on request from the authors.

Conflicts of Interest: The authors declare no conflict of interest.

References

1. Maldiney, T.; Bessière, A.; Seguin, J.; Teston, E.; Sharma, S.K.; Viana, B.; Adrie, J.J.B.; Pieter, D.; Michel, B.; Didier, G.; et al. The in vivo Activation of Persistent Nanophosphors for Optical Imaging of Vascularization, Tumours and Grafted Cells. *Nat. Mater.* **2014**, *13*, 418–426. [[CrossRef](#)]
2. Pan, Z.W.; Lu, Y.Y.; Liu, F. Sunlight-activated Long-persistent Luminescence in the Near-infrared from Cr³⁺-doped Zinc Gallogermanates. *Nat. Mater.* **2012**, *11*, 58–63. [[CrossRef](#)]
3. Hu, Z.F.; Ye, D.H.; Lan, X.J.; Zhang, W.; Luo, L.; Wang, X.H. Influence of Co-doping Si Ions on Persistent Luminescence of ZnGa₂O₄:Cr³⁺ Red Phosphors. *Opt. Mater. Express* **2016**, *6*, 1329. [[CrossRef](#)]
4. Lu, T. Micro and Nanoscale Characterization of Three Dimensional Surfaces. In *Basics and Applications*; Napoca Star Publishing House: Cluj-Napoca, Romania, 2015; pp. 21–27.
5. Abdukayum, A.; Chen, J.T.; Zhao, Q.; Yan, X.P. Functional Near Infrared-emitting Cr³⁺/Pr³⁺ Co-doped Zinc Gallogermanate Persistent Luminescent Nanoparticles with Superlong Afterglow for in vivo Targeted Bioimaging. *J. Am. Chem. Soc.* **2013**, *135*, 14125–14133. [[CrossRef](#)]
6. Shi, J.P.; Sun, X.; Li, J.L.; Man, H.Z.; Shen, J.S.; Yu, Y.K.; Zhang, H.W. Multifunctional Near Infrared-Emitting Long-Persistence Luminescent Nanoprobes for Drug Delivery and Targeted Tumor Imaging. *Biomaterials* **2015**, *37*, 260–270. [[CrossRef](#)]
7. Zou, R.; Gong, S.M.; Shi, J.P.; Jiao, J.; Wong, K.A.; Zhang, H.W.; Wang, J.; Su, Q. Magnetic-NIR Persistent Luminescent Dual-modal ZGOCS@MSNs@Gd₂O₃ Core-shell Nanoprobes for in vivo Imaging. *Chem. Mater.* **2017**, *29*, 3938–3946. [[CrossRef](#)]
8. Zou, R.; Huang, J.J.; Shi, J.P.; Huang, L.; Zhang, X.J.; Wong, K.L.; Zhang, H.W.; Jin, D.Y.; Wang, J.; Su, J. Silica Shell-assisted Synthetic Route for Mono-disperse Persistent Nanophosphors with Enhanced in vivo Recharged Near-infrared Persistent Luminescence. *Nano. Res.* **2017**, *10*, 2070–2082. [[CrossRef](#)]
9. Li, Z.J.; Zhang, Y.W.; Wu, X.; Huang, L.; Li, D.S.; Fan, W.; Han, G. Direct Aqueous-Phase Synthesis of Sub-10 nm “Luminous Pearls” with Enhanced in vivo Renewable Near-Infrared Persistent Luminescence. *J. Am. Chem. Soc.* **2015**, *137*, 5304–5307. [[CrossRef](#)]
10. Lu, Y.C.; Yang, C.X.; Yan, X.P. Radiopaque Tantalum Oxide Coated Persistent Luminescent Nanoparticles as Multimodal Probes for in vivo Near-infrared Luminescence and Computed Tomography. *Nanoscale* **2017**, *7*, 17929–17937. [[CrossRef](#)]

11. Wu, Y.L.; Li, Y.; Qin, X.X.; Qiu, J.R. A Multi-Functional Biomaterial with NIR Long Persistent Phosphorescence, Photo-Thermal Response and Magnetism. *Chem. Asian. J.* **2016**, *11*, 2537–2541. [[CrossRef](#)]
12. Li, Y.; Chen, R.C.; Li, Y.Y.; Sharafudeen, K.; Liu, S.J.; Wu, D.K.; Wu, Y.L.; Qin, X.X.; Qin, J.R. Folic Acid-Conjugated Chromium (III) Doped Nanoparticles Consisting of Mixed Oxides of Zinc, Gallium and Tin, and Possessing Near-infrared and Long Persistent Phosphorescence for Targeted Imaging of Cancer Cells. *Microchim. Acta.* **2015**, *182*, 1827–1834. [[CrossRef](#)]
13. Lv, Y.; Ding, D.D.; Zhuang, Y.X.; Feng, Y.S.; Shi, J.P.; Zhang, H.W.; Zhou, T.L.; Chen, H.M.; Xie, R.J. Chromium-Doped Zinc Gallogermanate@zeolitic Imidazolate Framework-8: A Multifunctional Nanoplatform for Rechargeable in vivo Persistent Luminescence Imaging and pH-Responsive Drug Release. *ACS. Appl. Mater. Interfaces* **2019**, *11*, 1907–1916. [[CrossRef](#)] [[PubMed](#)]
14. Zhu, Q.; Xiahou, J.Q.; Guo, Y.; Guo, Y.; Li, H.L.; Ding, C.; Wang, J.; Li, X.D.; Sun, X.D.; Li, J.G. Zn₃Ga₂Ge₂O₁₀:Cr³⁺ Uniform Microspheres: Template-Free Synthesis, Tunable Bandgap/Trap-Depth, and in vivo Rechargeable Near-Infrared Persistent Luminescence. *ACS. Appl. Bio. Mater.* **2019**, *2*, 577–587. [[CrossRef](#)] [[PubMed](#)]
15. Li, Y.; Zhou, S.F.; Li, Y.Y.; Sharafudeen, K.; Ma, Z.J.; Dong, G.P.; Peng, M.Y.; Qiu, J.R. Long Persistent and Photo-Stimulated Luminescence in Cr³⁺-doped Zn-Ga-Sn-O Phosphors for Deep and Reproducible Tissue Imaging. *J. Mater. Chem. C* **2014**, *2*, 2657–2663. [[CrossRef](#)]
16. Zhao, H.X.; Yang, C.X.; Yan, X.P. Fabrication and Bioconjugation of B^{III} and Cr^{III} Co-Doped ZnGa₂O₄ Persistent Luminescent Nanoparticles for Dual-Targeted Cancer Bioimaging. *Nanoscale* **2016**, *8*, 18987–18994. [[CrossRef](#)]
17. Duan, X.L.; Liu, J.; Wu, Y.C.; Yu, F.P.; Wang, X.Q. Structure and Luminescent Properties of Co²⁺/Cr³⁺ Co-doped ZnGa₂O₄ Nanoparticles. *J. Lumin.* **2014**, *153*, 361–368. [[CrossRef](#)]
18. Li, P.F.; Zhang, X.Y.; Zhang, J.R.; Qi, X.W.; Liu, X. Investigations of Thermal Stability and Spectroscopic Features of Sm³⁺ Doped Strontium Aluminate Glasses. *Coatings* **2022**, *12*, 3. [[CrossRef](#)]
19. Gai, C.L.; He, D.W.; Wang, Y.S.; Wang, J.G.; Li, J.M. Engineering of Halide Cation in All-Inorganic Perovskite with Full-Color Luminescence. *Coatings* **2021**, *11*, 330. [[CrossRef](#)]
20. Fang, J.; Liu, W.T.; Zhou, W.Y.; Zhu, C.; Ni, Y.R.; Fang, L.; Lu, C.H. Down-Conversion Polymer Composite Coatings with Multipeak Absorption and Emission. *Coatings* **2021**, *11*, 282. [[CrossRef](#)]
21. Patel, N.P.; Srinivas, M.; Modi, D.; Verma, V.; Venkata, K.; Murthy, R. Optimization of Luminescence Properties of Tb³⁺-Doped α -Sr₂P₂O₇ Phosphor Synthesized by Combustion Method. *Rare Met.* **2018**, *37*, 587–593. [[CrossRef](#)]
22. Sheoran, S.; Singh, K.; Tanwar, V.; Singh, S.; Samantilleke, A.; Singh, D. Synthesis and Spectroscopic Investigations of Trivalent Europium-doped Z₂Si₃O₈ (Z = Mg, Ca and Sr) Nanophosphors for Display Applications. *Rare Metals* **2021**, *40*, 2610–2617. [[CrossRef](#)]
23. Xie, J.H.; Wang, J.; Qiu, G.H.; Li, X.B.; Huang, W.T.; Zhang, R.R.; Lin, T.; Wang, L.X.; Zhang, Q.T. A Strategy to Achieve Efficient Green-Emission Dual-Mode Luminescence of Yb³⁺, Eu³⁺ Doped NaBiF₄. *Rare Metals* **2021**, *40*, 2040–2048. [[CrossRef](#)]
24. Allix, M.; Chenu, S.; Véron, E.; Poumeyrol, T.; Kouadri-Boudjelthia, E.A.; Alahraché, S.; Porcher, F.; Massiot, D.; Fayon, F. Considerable Improvement of Long-Persistent Luminescence in Germanium and Tin Substituted ZnGa₂O₄. *Chem. Mater.* **2013**, *25*, 1600–1606. [[CrossRef](#)]
25. Zhuang, Y.X.; Ueda, J.; Tanabe, S. Tunable Trap Depth in Zn(Ga_{1-x}Al_x)₂O₄: Cr, Bi Red Persistent Phosphors: Considerations of High-Temperature Persistent Luminescence and Photostimulated Persistent Luminescence. *J. Mater. Chem. C* **2013**, *1*, 7849–7855. [[CrossRef](#)]
26. Wang, Q.Q.; Zhang, S.Y.; Li, Z.W.; Zhu, Q. Near Infrared-Emitting Cr³⁺/Eu³⁺ Co-doped Zinc Gallogermanate Persistence Luminescent Nanoparticles for Cell Imaging. *Nanoscale Res. Lett.* **2018**, *13*, 64. [[CrossRef](#)]
27. Liu, F.; Liang, Y.J.; Pan, Z.W. Detection of Up-converted Persistent Luminescence in the Near Infrared Emitted by the Zn₃Ga₂GeO₈:Cr³⁺, Yb³⁺, Er³⁺ Phosphor. *Phys. Rev. Lett.* **2014**, *113*, 177401. [[CrossRef](#)]
28. Li, Y.; Gecevicius, M.; Qiu, J.R. Long Persistent Phosphors—from Fundamentals to Applications. *Chem. Soc. Rev.* **2016**, *45*, 2090–2136. [[CrossRef](#)] [[PubMed](#)]
29. Gong, Z.; Liu, Y.X.; Yang, J.; Yan, D.T.; Zhu, H.C.; Liu, C.G.; Xu, C.S.; Zhang, H. A Pr³⁺ Doping Strategy for Simultaneously Optimizing the Size and Near Infrared Persistent Luminescence of ZGGO:Cr³⁺ Nanoparticles for Potential Bio-imaging. *Phys. Chem. Chem. Phys.* **2017**, *19*, 24513–24521. [[CrossRef](#)]
30. Shannon, R.D. Revised Effective Ionic Radii and Systematic Studies of Interatomic Distances in Halides and Chalcogenides. *Acta. Cryst. A* **1976**, *32*, 751–767. [[CrossRef](#)]
31. Kang, H.I.; Kim, J.S.; Lee, M.; Bahng, J.H.; Choi, J.C.; Park, J.K.; Kim, G.C.; Kim, T.W.; Hwang, Y.H.; Mho, S.I.; et al. Tunable Color Emission of ZnGa₂O₄:Si⁴⁺ Phosphors with Enhanced Brightness Due to Donor Formation. *Solid State Commun.* **2002**, *122*, 633–636. [[CrossRef](#)]
32. Gorkom, G.; Haanstra, J.; Boom, H. Infrared and Raman Spectra of the Spinel ZnGa₂O₄. *J. Raman. Spectrosc.* **1973**, *1*, 513–519. [[CrossRef](#)]
33. López, S.; Romero, A. First-Principles Study of the High-Pressure Phase Transition in ZnAl₂O₄ and ZnGa₂O₄: From Cubic Spinel to Orthorhombic Post-Spinel Structures. *Phys. Rev. B* **2009**, *79*, 214103. [[CrossRef](#)]
34. Wu, Y.L.; Li, Y.; Qin, X.X.; Chen, R.C.; Wu, D.K.; Liu, S.J.; Qin, J.R. Near-Infrared Long-Persistent Phosphor of Zn₃Ga₂Ge₂O₁₀:Cr³⁺ Sintered in Different Atmosphere. *Spectrochim. Acta A Mol. Biomol. Spectrosc.* **2015**, *151*, 385–389. [[CrossRef](#)]
35. Zhu, Q.; Xiahou, J.Q.; Li, X.D.; Sun, X.D.; Li, J.G. Defect Cluster Engineering in ZnGa_{2-x}(Mg/Ge)_xO₄:Cr³⁺ Nanoparticles for Remarkably Improved NIR Persistent Luminescence. *J. Am. Ceram. Soc.* **2021**, *104*, 4594–4605. [[CrossRef](#)]

36. Xiahou, J.Q.; Zhu, Q.; Zhu, L.; Li, S.Y.; Li, J.G. Local Structure Regulation in Near-Infrared Persistent Phosphor of $\text{ZnGa}_2\text{O}_4:\text{Cr}^{3+}$ to Fabricate Natural-Light Rechargeable Optical Thermometer. *ACS. Appl. Electron. Mater.* **2021**, *3*, 3789–3803. [[CrossRef](#)]
37. Xiahou, J.Q.; Zhu, Q.; Zhu, L.; Huang, S.; Zhang, T.; Sun, X.D.; Li, J.G. Lattice-Site Engineering in $\text{ZnGa}_2\text{O}_4:\text{Cr}^{3+}$ through Li^+ Doping for Dynamic Luminescence and Advanced Optical Anti-Counterfeiting. *J. Mater. Chem. C* **2022**, *10*, 7935. [[CrossRef](#)]
38. Lin, X.H.; Zhang, R.L.; Tian, X.M.; Li, Y.; Du, B.U.; Nie, J.M.; Li, Z.Z.; Chen, L.; Ren, J.J.; Qiu, J.R.; et al. Coordination Geometry-dependent Multi-Band Emission and Atypically Deep-Trap-Dominated NIR Persistent Luminescence from Chromium-Doped Aluminates. *Adv. Optical Mater.* **2018**, *6*, 1701161. [[CrossRef](#)]
39. Gupta, P.; Kumar, M.; Nagarajan, R. Interplay Between Defects and Cation Nonstoichiometry in Lithium-Substituted CdGa_2O_4 Leading to Multifunctional Behavior. *J. Phys. Chem. C* **2018**, *122*, 22094–22105. [[CrossRef](#)]